2014

Constructing tailored isoprenoid products by structure-guided modification of geranylgeranyl reductase

Yan Kung
Bryn Mawr College, ykung@brynmawr.edu

Ryan P. McAndrew

Xinkai Xie

Charlie C. Liu

Jose H. Pereira

See next page for additional authors

Custom Citation

Kung, Y., McAndrew, R. P., Xinkai, X., Liu, Charlie C., Pereira, J. H., Adams, P. D., & Keasling, J. D. "Constructing Tailored Isoprenoid Products by Structure-Guided Modification of Geranylgeranyl Reductase." *Structure* 22.7 (2014): 1028-1036. DOI: 10.1016/j.str.2014.05.007

Authors
Yan Kung, Ryan P. McAndrew, Xinkai Xie, Charlie C. Liu, Jose H. Pereira, Paul D. Adams, and Jay D. Keasling

Constructing tailored isoprenoid products by structure-guided modification of geranylgeranyl reductase

Yan Kung,[1-3,7] Ryan P. McAndrew,[1,2,7] Xinkai Xie,[1-2] Charlie C. Liu,[4] Jose H. Pereira,[1-2] Paul D. Adams,[1,2,5] and Jay D. Keasling[1,2,5,6]

1. Physical Biosciences Division, Lawrence Berkeley National Laboratory, 1 Cyclotron Road, Berkeley, CA 94720, USA
2. Joint BioEnergy Institute, 5885 Hollis Street, Emeryville, CA 94608, USA
3. Department of Chemistry, Bryn Mawr College, 101 North Merion Avenue, Bryn Mawr, PA 19010, USA
4. Department of Molecular and Cell Biology,
5. Department of Bioengineering,
6. Department of Chemical and Biomolecular Engineering
   University of California, Berkeley, CA 94720, USA
7. These authors contributed equally to this work

SUMMARY

The archaeal enzyme geranylgeranyl reductase (GGR) catalyzes hydrogenation of carbon-carbon double bonds to produce the saturated alkyl chains of the organism's unusual isoprenoid-derived cell membrane. Enzymatic reduction of isoprenoid double bonds is of considerable interest both to natural products researchers and to synthetic biologists interested in the microbial production of isoprenoid drug or biofuel molecules. Here we present crystal structures of GGR from *Sulfolobus acidocaldarius*, including the structure of GGR bound to geranylgeranyl pyrophosphate (GGPP). The structures are presented alongside activity data that depict the sequential reduction of GGPP to H_6GGPP via the intermediates H_2GGPP and H_4GGPP. We then modified the enzyme to generate sequence variants that display increased rates of H_6GGPP production or are able to halt the extent of reduction at H_2GGPP and H_4GGPP. Crystal structures of these variants not only reveal the structural bases for their altered activities; they also shed light onto the catalytic mechanism employed.

INTRODUCTION

Isoprenoids, also called terpenes and terpenoids, form a large and structurally diverse class of natural products that display a multitude of biological functions. Isoprenoids are also a major target in synthetic biology for the microbial production of biofuels, medicines, and other commodity chemicals, such as the anti-malarial drug precursor artemisinic acid (Ro et al., 2006), the taxol precursor taxadiene (Ajikumar et al., 2010), the biodiesel precursors farnesene and bisabolene (Peralta-Yahya et al., 2011; Renninger and McPhee, 2008), and the carotenoid lycopene (Alper et al., 2005; Farmer and Liao, 2000), which have all been produced in engineered microbes. All isoprenoids are constructed from the isomeric five-carbon (C_5) building blocks isopentenyl pyrophosphate (IPP) and dimethylallyl pyrophosphate (DMAPP), which are generated by the mevalonate pathway or the 1-deoxy-D-xylulose 5-phosphate (DXP) pathway. IPP and DMAPP are first condensed by prenyltransferases to form isoprenoid intermediates of varying chain lengths: geranyl pyrophosphate (GPP, C_{10}), farnesyl pyrophosphate (FPP, C_{15}), or geranylgeranyl pyrophosphate (GGPP, C_{20}). Dedicated terpene synthases then convert these intermediates into monoterpene (C_{10}), sesquiterpene (C_{15}), or diterpene (C_{20}) products using carbocation-based structural rearrangements, which use the double bonds of GPP, FPP, and GGPP as nucleophiles to cyclize, adjust, and rearrange the carbon skeleton. Terpene synthases are thus primarily responsible for the incredible structural diversity of isoprenoid products.

Isoprenoids also form the major component of membrane phospholipids in archaea. Unlike bacterial or eukaryotic membranes, which are primarily composed of fatty acyl chains linked to phosphoglycerol by ester bonds, archaeal membranes are

composed of isoprenoid-derived chains linked to phosphoglycerol by ether bonds. Here, two geranylgeranyl chains from GGPP are first tethered to phosphoglycerol in the molecule 2,3-di-*O*-geranylgeranylglyceryl phosphate (DGGGP). Next, the enzyme geranylgeranyl reductase (GGR) performs the remarkable sixteen-electron reduction of all DGGGP double bonds to produce saturated alkyl chains using flavin adenine dinucleotide (FAD) as a cofactor. Interestingly, prior studies have shown that GGR from *Sulfolobus acidocaldarius* (SaGGR) is able to reduce three out of the four double bonds of the non-native substrate GGPP to produce the hexahydro-product, H_6GGPP (Sato et al., 2008). Although GGR from *Thermoplasma acidophilum* (TaGGR) can utilize NADPH as a direct electron source (Nishimura and Eguchi, 2006), SaGGR cannot directly use NADPH or NADH (Sato et al., 2008), and neither its ultimate *in vivo* source of electrons nor any potential redox protein partners are currently known. In addition, crystal structures of SaGGR and TaGGR have been previously determined (Sasaki et al., 2011; Xu et al., 2010). Although SaGGR was co-crystallized with 1.0 mM GGPP, the electron density was discontinuous and inconsistent with GGPP; instead, *n*-nonane and pyrophosphate were modeled (Sasaki et al., 2011).

In addition to being of considerable biological interest due to its key role in archaeal membrane biosynthesis, GGR also holds great promise for isoprenoid production in engineered microbes, as its isoprenoid double bond reduction activity would allow for greater tailoring of the final product. Here, reduction of isoprenoid double bonds would decrease the reactivity and sensitivity to oxidation of the target compound, in addition to altering its physicochemical properties. Such features are especially beneficial for isoprenoid-based biofuels; in fact, microbially produced

farnesene and bisabolene must first be hydrogenated to farnesane and bisabolane, respectively, to become practical biodiesel alternatives (Peralta-Yahya et al., 2011; Renninger and McPhee, 2008). Further, *in vivo* enzymatic hydrogenation has several advantages over chemical hydrogenation. First, the capital cost of chemical hydrogenation would be eliminated by simply using a strain that expresses a requisite hydrogenation enzyme. In addition, *in vivo* hydrogenation would be valuable in host organisms that use the mevalonate pathway in anaerobic fermentation, where redox balance becomes a serious issue. Here, GGR could play an important role in consuming excess reducing equivalents and regenerating oxidized $NAD(P)^+$. Enzymatic reduction of double bonds within the biosynthetic pathway also raises the possibility of using an engineered enzyme that could selectively reduce specific double bonds, as opposed to chemical hydrogenation of an isolated final product that would likely reduce all double bonds. Despite its potential, however, the use of GGR in synthetic biology for the reduction of isoprenoids has remained largely unexplored and unstudied, as GGR not only awaits further biochemical and structural characterization, but practical GGR enzymes must also be identified or engineered.

Here, we present the structure of SaGGR bound with GGPP, along with activity data on GGPP reduction using a new enzymatic assay based on mass spectrometry. Using these results, we performed structure-guided design of SaGGR to alter the reaction rate and to tailor the extent of GGPP reduction. We generated SaGGR variants that exhibit increased rates of H_6GGPP production and also identified additional SaGGR variants that are capable of halting GGPP reduction at the dihydro-product, H_2GGPP, and at the tetrahydro-product, H_4GGPP. Crystal structures of these SaGGR variants bound to GGPP

reveal the structural bases for their altered activities and further illuminate the catalytic mechanism of GGR, an enzyme of both biological interest and of potential utility in the microbial production of isoprenoid compounds.

RESULTS AND DISCUSSION

Structure and activity of wild-type SaGGR

Crystal structures of SaGGR were determined to high resolution bound to phosphatidylglycerol (PG) and to GGPP. During the preparation of this manuscript, the structure of SaGGR in complex with a non-physiological ligand was published (Sasaki et al., 2011), which described the overall structure of SaGGR in detail. Briefly, SaGGR is a monomer composed of two functional domains: an FAD-binding Rossmann–type fold domain (residues 1–74) and a ligand–binding domain (residues 75–453) (Figure 1). The overall structure closely resembles TaGGR (Xu et al., 2010) with an r.m.s.d of 1.5 Å over 350 residues. SaGGR possesses an additional 60 amino acids at the C-terminus that TaGGR does not. This region is α-helical in nature and is contiguous with the ligand-binding domain; it does not clearly form a domain distinct from the ligand-binding domain.

Alhough our crystals were prepared without substrate, additional density was observed in the active site (Figure S1A). Lipid analysis later revealed this to be PG, which, while not a GGR substrate, has a similar structure to the native substrate DGGGP (Figure S1B), and it is likely that the membrane lipid remained bound during purification. The two chains of PG bind in separate cavities (Figure S1A), and only one chain, which interacts with the FAD, appears to be bound in a catalytically relevant manner. The

chains are separated by Y215 and a loop region (290-301). The phosphate in the lipid head group forms salt bridge interactions with H55 and H297 and hydrogen bonds with Y340 and N294.

We also co-crystallized SaGGR with GGPP (Figures 1 and 2A). Unexpectedly, electron density was resolved for three separate molecules of GGPP (Figure S2A). Similar to PG, only one GGPP molecule ($GGPP_1$) appears to be bound in a catalytically competent manner. The hydrophobic chain from the second GGPP molecule ($GGPP_2$) is bound in a manner similar to the second chain from PG. The third GGPP molecule ($GGPP_3$) binds SaGGR alongside $GGPP_2$ within the same cavity. Although electron density was clear for all GGPP alkyl chains, disorder was observed in the pyrophosphate head groups of some GGPP binding sites. Only the model for $GGPP_1$ includes both phosphate groups of the pyrophosphate moiety. The model for $GGPP_2$ contains a single phosphate, and $GGPP_3$ is modeled without any phosphates, and it is possible that GGPP became dephosphorylated during the course of crystallization. Therefore, a mixture of substrates with different degrees of phosphorylation may be present and only the phosphates that could be confidently fit into the electron density were included in the model. However, to avoid confusion all GGPP-based ligands will be referred to as GGPP.

The pyrophosphate moiety of $GGPP_1$ binds SaGGR in a completely different manner than the phosphate in PG. The β-phosphate forms a hydrogen bond with the backbone carbonyl of N90, while the phosphate of $GGPP_2$ shows similar binding interactions as the phosphate from PG: salt bridges are formed between the pyrophosphate moiety and H55, H297, and K343 and hydrogen bonds occur with Y340

and N294 (Figure 2A). In all three GGPP molecules, the alkyl chains are bound by hydrophobic residues of the protein.

In the bound $GGPP_1$ molecule that represents reactive GGPP binding, the terminal double bond at the opposite end from the pyrophosphate group, the Δ^{14} double bond, sits directly facing the N^5 position of FAD (3.1 Å) from which it accepts a hydride for its reduction. Interestingly, the GGPP methyl group adjacent this double bond is located in the space formed between the conserved residues F219 and W217 (Figure 2B). Because all other geranylgeranyl double bonds of the native DGGGP substrate must also be reduced by FAD in the reaction cycle, all double bonds would be positioned in a similar manner, with their adjacent, branching methyl groups wedged between F219 and W217. In this way, these two residues are involved in properly orienting the substrate in order to present the double bond to $FADH_2$ for reduction.

Our activity studies of wild-type (WT) SaGGR with GGPP reveal a six-electron reduction of GGPP to H_6GGPP, via the intermediates H_2GGPP and H_4GGPP, with an optimal temperature of approximately 50°C and an optimal pH of approximately 5.5 (Figure S3). In the reaction, GGPP (m/z: 449.2) is reduced first to H_2GGPP (m/z: 451.2), which is observed only initially and in low levels (Figure 3A and Figure S4). Subsequently, a more significant build up of H_4GGPP (m/z: 453.2) occurs, attaining a maximum accumulation after approximately 3 min. This H_4GGPP intermediate is then consumed with concomitant formation of the product, H_6GGPP (m/z: 455.2). The fully reduced form, H_8GGPP (expected m/z: 457.2), was not detected (Figure S4). These findings are consistent with prior SaGGR results, which also identified H_6GGPP as the product with the greatest degree of GGPP reduction (Sato et al., 2008). Time course

experiments yield a maximal apparent rate (v_{app}) of H_6GGPP formation of 12 ± 2 μM min^{-1} and an apparent rate constant (k_{app}) for H_6GGPP of 0.40 ± 0.05 min^{-1} (Table 2). Another useful metric to assess the rate of reaction is the time required to reach 50% maximal conversion (t_{50}) of GGPP to H_6GGPP, which was 6.3 min.

Engineered GGR variants with altered activity

Using our crystal structure of GGPP-bound WT SaGGR, we designed mutant enzymes with the goal of altering enzyme activity. We then determined crystal structures for engineered variants with improved activity or those that may provide insight into the enzyme mechanism. One objective was to engineer SaGGR to fully reduce the non-native GGPP substrate, as reduction to H_8GGPP had not been observed in the WT enzyme. Because the crystal structure depicted the site of the terminal, Δ^{14} GGPP double bond poised for reduction by FAD (Figure 2B), and because our activity studies showed that three of the four double bonds are reduced, we speculated that the remaining, unreduced double bond was the double bond closest to the pyrophosphate, the Δ^2 double bond. This judgment was also reached in prior SaGGR experiments with GGPP (Sato et al., 2008). Therefore, we targeted the largely hydrophobic residues lining the GGPP-binding channel for mutation to polar or positively charged residues, with the aim of bringing the pyrophosphate moiety deeper into the active site. We also mutated these residues to those with smaller side chains in order to better accommodate the pyrophosphate head group. Another objective was to inhibit unproductive binding of GGPP to the auxiliary binding sites observed in the crystal structure as $GGPP_2$ and $GGPP_3$ (Figure 2A). Here, we

mutated residues pointed towards these binding channels to bulkier hydrophobic residues in order to sterically hinder non-catalytic GGPP binding.

Of the >30 SaGGR variants tested, none fully reduced GGPP to H_8GGPP. However, several mutants displayed interesting activity profiles that significantly differed from WT SaGGR. Two mutants, I206F and L377H, exhibited faster overall reduction of GGPP to H_6GGPP compared to WT SaGGR (Figure 3F). Time course experiments gave v_{app} of H_6GGPP for I206F and L377H mutants of 16 ± 4 and 28 ± 11 μM min^{-1}, respectively, k_{app} of 0.53 ± 0.14 and 0.94 ± 0.36 min^{-1}, respectively, and t_{50} of 5.0 and 3.7 min, respectively (Table 2). As with the wild-type enzyme, the I206F and L377H mutants reduce GGPP first by rapid formation and consumption of H_2GGPP, followed by an initial buildup of H_4GGPP that precedes reduction to H_6GGPP, the final product (Figures 3B-3C, Figure S4).

The I206F mutation was intended to obstruct non-catalytic GGPP binding in the $GGPP_2$ and $GGPP_3$-binding sites determined in the WT crystal structure. The structure of this variant confirms that F206 partially occludes the second cavity (Figure 4A and Figure S2B). Therefore, the catalytically inactive binding conformations are unavailable to GGPP. Weak electron density was observed for the $GGPP_1$ position. However, the ligand could not be modeled with full confidence and was not included in the final structure (Figure S2B).

For the L377H mutant, the WT SaGGR crystal structure shows L377 residing on the enzyme's surface, at the opening of the catalytic GGPP binding site and directly adjacent the pyrophosphate head group. Mutation of this residue to histidine was intended to stabilize GGPP binding in its catalytic binding site. Indeed, H377 of the mutant forms

a salt bridge with the GGPP pyrophosphate (Figure 4B), thereby improving substrate binding. Apart from its interaction with H377, GGPP binds to the L377H in the same way as it binds to the WT enzyme, with the terminal, Δ^{14} double bond directly adjacent the N^5 of FAD (Figure 4B).

Interestingly, a double I206F/L377H mutant produced H_6GGPP faster than either of the single I206F or L377H mutants (Figure 4, Figure S4), with v_{app}, $k_{app,}$ and t_{50} for H_6GGPP of 29 ± 3 μM min^{-1}, 0.95 ± 0.09 min^{-1}, and 2.6 min, respectively (Table 2). Overall, the I206F/L377F mutant was the fastest SaGGR variant tested, generating H_6GGPP approximately 2.4-fold faster than the WT enzyme. The crystal structure of the I206H/L377H double mutant correspondingly depicts the features of both I206F and L377F single-mutant structures described above combined in the same structure, with GGPP also bound with its Δ^{14} double bond directly adjacent the N^5 of FAD. From these data, it appears that the rate-enhancing effects of the individual mutations are additive.

On the other hand, another mutant, G91H, halts the reduction of GGPP at H_2GGPP (Figure 3D, Figure S4). After reaching maximal H_2GGPP levels after approximately 10 min, only a very small quantity of H_2GGPP is reduced further to H_4GGPP or to H_6GGPP (Figures 3D and 3F). This is in contrast to the H_6GGPP-producing WT, I206F, L377H, and I206F/L377H enzymes discussed above, which do not accumulate appreciable levels of H_2GGPP at any point during the reaction. The G91H mutant displays v_{app}, k_{app}, and t_{50} for H_2GGPP of 25 ± 4 μM min^{-1}, 0.83 ± 0.14 min^{-1}, and 3.0 min, respectively (Table 2). Notably, the G91H t_{50} for H_2GGPP is slightly greater than the I206F/L377H t_{50} for H_6GGPP, indicating that the fastest H_6GGPP producer performs three reductions of GGPP (from GGPP to H_6GGPP) faster than G91H performs

one reduction (from GGPP to H_2GGPP). Interestingly, although mutation of both G91 and L377 to histidine gives completely different reactive outcomes, forming H_2GGPP and H_6GGPP products, respectively, both residues in the WT SaGGR crystal structure are located at a similar position on the surface of the enzyme, at the opening of the same GGPP binding site. In fact, G91 and L377 sit directly across the opening from each other, with the GGPP pyrophosphate group located in the center. Our crystal structure of the G91H variant shows that, like H377 in the L377H mutant, H91 similarly forms a salt bridge with the GGPP pyrophosphate (Figure 4C). However, unlike in the L377H structure, GGPP in the G91H structure is bound in a different position, where the GGPP substrate has slid farther into the protein cavity, placing the Δ^6 double bond instead of the Δ^{14} double bond directly adjacent N^5 of FAD.

Going one reduction further than the G91H mutant, another SaGGR variant, the F219L mutant, ceases GGPP reduction at H_4GGPP without significant conversion to H_6GGPP (Figure 3E, Figure S4). Interestingly, F219 is a conserved residue that is thought to serve a role in substrate binding as described above, where the GGPP methyl group flanking the reduced double bond is wedged between F219 and the conserved W217 in order to correctly orient the substrate double bond for reduction by $FADH_2$. Mutation of F219 to leucine was intended to provide more room in the substrate-binding channel for the pyrophosphate head of GGPP to move farther into the active site without compromising the hydrophobic environment. The crystal structure of the F219L mutant confirms that this is the case (Figure 4D). In experiments with the F219L mutant, a small buildup of H_2GGPP is observed after the reaction is initiated, followed by the production of H_4GGPP, with v_{app}, k_{app}, and t_{50} for H_4GGPP of 23 ± 5 μM min^{-1}, 0.78 ± 0.15 min^{-1},

and 3.0 min, respectively (Table 2), without significant reduction to H_6GGPP (Figure 3F). It is possible that the increased size of the active site cavity no longer provides sufficient van der Waals interactions for efficient binding and further reduction of the substrate.

Using simple mutations derived from structure-guided design, we have enhanced and expanded the catalytic repertoire of SaGGR activity towards a non-native substrate, GGPP. Three mutants (I206F, L377H, and I206F/L377H) exhibit faster production of H_6GGPP than the WT, increasing the overall rate of product formation by up to 2.4-fold. Two other mutants selectively arrest the progression of GGPP reduction at different intermediate stages, with G91H producing H_2GGPP and F219L producing H_4GGPP at rates comparable to H_6GGPP formation in the fastest H_6GGPP-producing mutants. These mutants provide customized degrees of hydrogenation for the key isoprenoid intermediate GGPP. Overall, these results highlight the power of structure-guided design in tailoring the kinetic and reactive outcomes of enzymes through small changes in the protein sequence.

Mechanistic implications

Our structures of engineered SaGGR variants not only reveal the structural bases for their altered reactivities, they also help illuminate the enzymatic mechanism employed. As these structures capture snapshots of the GGPP substrate at different stages during the reaction, the mechanism by which GGR reduces successive double bonds of the same substrate may be more deeply explored.

As discussed, the GGPP-bound crystal structures of the H_6GGPP-producing enzymes (WT and L377H GGR) show the GGPP Δ^{14} double bond directly adjacent the

N^5 position of the FAD cofactor. On the other hand, the structure of the G91H mutant, which reduces just one double bond to form H_2GGPP, shows that formation of the salt bridge between H91 and the $GGPP_1$ pyrophosphate now places the Δ^6 double bond adjacent N^5 of FAD. These results suggest that the first double bond to be reduced is the Δ^6 double bond, while the Δ^{14} double bond is the last double bond to be reduced. Here, through its interaction with the $GGPP_1$ pyrophosphate, the G91H mutant obstructs translocation of the H_2GGPP intermediate to inhibit further reduction (Figure 4C). This reduction sequence implies that the double bond between Δ^6 and Δ^{14}, the Δ^{10} double bond, is the second to be reduced. As H_8GGPP is not formed by any enzyme, these data suggest that the Δ^2 double bond is left intact, consistent with prior studies (Sato et al., 2008). In all, our SaGGR structures indicate that GGR first reduces GGPP at the Δ^6 double bond, then at Δ^{10}, and finally at Δ^{14} (Fig. S2C).

Interestingly, in the structure of the F219L mutant which performs two reductions of GGPP to H_4GGPP, $GGPP_1$ is bound in the same manner as in the WT and L377H structures, with the Δ^{14} double bond adjacent the N^5 of FAD (Figure 4D). This observation suggests that the F219L variant first reduces the Δ^{10} double bond before reducing the Δ^{14} double bond, giving the $GGPP_1$ position represented in the structure and consistent with the order of reduction described above.

Although the order of double bond reduction is suggested by the structures, the structures do not indicate whether GGR employs a processive mechanism or not, that is whether the enzyme successively reduces the double bonds of a single substrate molecule before moving on to the next, or whether H_2GGPP or H_4GGPP intermediates dissociate from the enzyme before the final H_6GGPP product is made. However, the mass

spectrometry data indicate that the mechanism of H_6GGPP formation is not processive, as before H_6GGPP is made, GGPP continues to be consumed to form H_2GGPP and H_4GGPP, allowing a clear buildup of the intermediate H_4GGPP. Therefore, H_4GGPP must dissociate from the enzyme, enabling the next molecule of GGPP to bind and be reduced, before reduction of H_4GGPP to H_6GGPP proceeds. However, it is difficult to determine whether the first two GGPP reductions, first to H_2GGPP and then to H_4GGPP, are processive. On the one hand, a processive mechanism to H_4GGPP appears to be supported by the data, as no significant buildup of H_2GGPP is observed. However, it is also possible that the second reaction to form H_4GGPP is sufficiently faster than the first to allow rapid reduction of H_2GGPP, making the first step rate-determining. Additional studies may be performed to further explore the processivity of GGR reduction. Although it is possible that the native reaction with DGGGP may not follow the same mechanism, this is unlikely as the enzyme catalyzes the reduction of the same geranylgeranyl moiety of both GGPP and DGGGP substrates.

Conclusions

The crystal structure of WT SaGGR bound with GGPP was determined, which unexpectedly showed three binding sites for GGPP and revealed how the enzyme orients double bonds to be reduced by the bound FAD cofactor. Structure-guided design of the enzyme yielded SaGGR variants that enhanced the rate of H_6GGPP product formation. Interestingly, additional mutants were observed to arrest the degree of GGPP reduction at H_2GGPP and H_4GGPP. Crystal structures of these variants reveal the structural bases for their altered activities, in addition to providing insight into the SaGGR mechanism.

With these GGR variants, the degree of GGPP reduction can be customized enzymatically, a feature that is particularly useful in synthetic biology. As GGPP is a key intermediate in the production of countless isoprenoid-derived products, including all diterpenes, retinoids, and carotenoids, modified GGRs such as these may be used to tailor the degree of hydrogenation and alter the isoprenoid product profile. Because terpene synthases rely on double bonds at specific positions to rearrange the carbon skeleton, the use of modified GGRs to selectively reduce specific GGPP double bonds can re-direct the reactive outcome towards different products. In addition, it is useful that, as with the WT enzyme, no SaGGR variants reduced the Δ^2 double bond, as a double bond in this position is necessary for providing the resonance-stabilized allylic carbocation in subsequent reactions that involve removal of the pyrophosphate group; if the Δ^2 double bond were reduced, the resulting H_8GGPP would be a dead-end product. As our engineered enzymes exhibit altered product profiles, these studies pave the way for the use of modified GGRs in the microbial production of tailored isoprenoid products.

EXPERIMENTAL PROCEDURES

Plasmid construction

A codon-optimized gene encoding SaGGR was synthesized (Genscript USA, Inc.) with flanking *Nde* I and *BamH* I restriction sites. The gene cassettes were digested with *Nde* I amd *BamH* I and ligated into pSKB3, a plasmid which confers kanamycin resistance and encodes a TEV protease-cleavable N-terminal hexahistadine tag to aid in protein purification. Mutant SaGGR constructs were made by standard oligonucleotide-directed PCR mutagenesis using pSKB3-SaGGR as a template and the complementary

oligonucleotides listed in Table S1 as primers. All constructs were verified by DNA sequencing (Quintara Biosciences).

Protein overexpression and purification

Plasmids were transformed into *Escherichia coli* BLR(DE3) or Rosetta2(DE3)pLysS cells for overexpression. Cells were grown in LB or TB medium supplemented with 50 μg/mL kanamycin, or 50 μg/mL kanamycin plus 34 μg/mL chloramphenicol in the case of the Rosetta2(DE3)pLysS cells, at 37°C to an OD_{600} of 0.5-0.7, when the cultures were transferred to 18°C. Overnight overexpression was then induced with 0.1-0.5 mM isopropyl β-D-1-thiogalactopyranoside (IPTG). Cells were harvested by centrifugation at 5,000 × *g* for 15 min at 4°C, flash-frozen in liquid nitrogen, and stored at -80°C until use.

Cells were thawed and resuspended in Lysis Buffer (20 mM NaH_2PO_4, pH 7.4, 200 mM NaCl, 20 mM imidazole), and phenylmethylsulfonyl fluoride (PMSF) and Benzonase (EMD Millipore) were added at 0.5 mM and 5 U/mL concentrations, respectively. Cell lysis was performed by sonication, and cell debris was pelleted by centrifugation at 50,000 × *g* for 30 min. Soluble extracts were incubated with Ni-NTA resin for 1 h at 4°C and loaded onto a column. The flow-through was discarded and the resin was washed with approximately 10 column volumes of Lysis Buffer containing 40 mM imidazole. Protein was eluted with Lysis Buffer containing 250 mM imidazole, and yellow fractions representing FAD-bound GGR were collected and pooled. The purified protein was buffer-exchanged into Lysis Buffer by either overnight dialysis or cycles of protein concentration and dilution.

To remove the hexahistidine tag, EDTA (0.5 mM), DTT (1 mM), and hexahistidine-tagged TEV protease (approximately 1:100 molar ratio compared to GGR) were added. Reactions were mixed and incubated overnight at room temperature. TEV protease, cleaved hexahistidine tags, and any remaining uncleaved SaGGR were removed by passing the solution through Ni-NTA resin pre-equilibrated with Lysis Buffer and collecting the flow-through. Successful cleavage of the tag and the purity of SaGGR were assessed by SDS-PAGE. The protein was then buffer exchanged into 20 mM NaH_2PO_4, pH 7.4, using a Sephadex G-25 column (GE Healthcare) and concentrated to 7-10 mg/mL. Final protein concentrations were determined by the Bradford method (Bradford, 1976) and by the absorbance at 280 nm using a calculated extinction coefficient, ε, of 82,100 M^{-1} cm^{-1}. Protein samples were either used directly or aliquoted, flash frozen in liquid nitrogen, and stored at -80°C until use.

Enzymatic assays

Reactions were performed at least in triplicate and contained 100 mM 2-(*N*-morpholino)ethanesulfonic acid (MES) pH 5.5, 20 mM sodium dithionite, 200 μM FAD, and 100 μM GGPP. Reaction mixtures were pre-heated to 50°C and initiated by the addition of 30 μM purified SaGGR. The reactions were mixed and incubated at 50°C for varying durations. Reactions were quenched and extracted with an equal volume of *n*-butanol. In experiments that determined the pH optimum, 100 mM citric acid/sodium citrate (pH 2.5-5.0), MES (pH 5.5-6.5), and NaH_2PH_4/Na_2HPO_4 (pH 7.0-8.0) were used as reaction buffers in place of MES, pH 5.5. In experiments that determined the

temperature optimum, reaction mixtures were pre-heated to varying temperatures on a thermal cycler, and purified WT SaGGR was added to initiate the reaction.

To screen SaGGR variants for the extent of GGPP reduction, the organic phase was analyzed by LC-MS. Reaction products were separated by HPLC (Agilent Technologies) using a 2.1×150 mm ZIC-pHILIC column (EMD Millipore) and an isocratic elution of 64% v/v acetonitrile and 36% v/v 50 mM ammonium acetate in water at a flow rate of 0.15 mL/min at 40°C. The HPLC system was coupled to a triple quadrupole mass spectrometer (Applied Biosystems). Electrospray ionization (ESI) was conducted in the negative ion mode, and single ion monitoring (SIM) was used for the detection of $[M-H]^-$ ions at approximately 449, 451, 453, and 455 m/z, representing GGPP, H_2GGPP, H_4GGPP, and H_6GGPP, respectively.

To quantify GGPP and its reactions products for WT SaGGR and select mutants, the organic phase was analyzed by LC-TOF MS. Reaction products were separated by HPLC using a ZIC-pHILIC column (Merck SeQuant, via The Nest Group, Inc., MA) and an isocratic elution of 62% v/v acetonitrile and 37% 50 mM ammonium carbonate in water at a flow rate of 0.2 mL/min at 40°C. The HPLC system was coupled to a time-of-flight mass spectrometer (Agilent Technologies). ESI was conducted in the negative ion mode, and MS experiments were carried out in full scan mode, at 0.86 spectra/s for the detection of $[M-H]^-$ ions. The instrument was tuned for a range of 50-1700 m/z. Data acquisition and processing were performed by the MassHunter software package. Analytes were quantified using seven-point calibration curves (1.5625-100 μM GGPP) whose R^2 coefficients were >0.99.

The total concentrations of all reaction products varied between samples, perhaps due to differences in extraction efficiency. Therefore, instead of directly establishing absolute concentrations for each product, relative concentrations were first determined and as a percentage of the total products for each sample. Apparent reaction rates, v_{app}, for each sample were thus determined initially in units of % min^{-1}, which were then converted to μM min^{-1} given the initial substrate concentration of 100 μM. The validity of this unit conversion rests only on the assumption that GGPP, H_2GGPP, H_4GGPP, and H_6GGPP extract with approximately equal efficiencies, which we believe is reasonable.

Crystallization

Purified WT and mutant SaGGR were concentrated to ~10 mg/ml in a buffer containing 25 mM HEPES pH 7.4. Crystallization screening was carried out on a Phoenix robot (Art Robbins Instruments, Sunnyvale, CA) using a sparse matrix screening method (Jancarik and Kim, 1991). Proteins were crystallized by sitting-drop vapor diffusion in drops containing a 1:1 ratio of protein solution and 0.1 M Tris pH 7.5, 10% PEG 3350 and 0.2 M L-proline. An additional 5 mM GGPP was added to the crystallization buffer to obtain the ligand-bound crystals. Yellow crystals were observed within two days. For data collection, crystals were flash frozen in liquid nitrogen from a solution containing mother liquor and 10% glycerol.

X-ray data collection and structure determination

The X-ray diffraction data for SaGGR were collected at the Berkeley Center for Structural Biology beam lines 8.2.1 and 8.2.2 of the Advanced Light Source at Lawrence

Berkeley National Laboratory. Diffraction data were recorded using ADSC Q315R detectors (Area Detector Systems Corporation, San Diego, CA). Processing of image data was performed using the HKL2000 suite of programs (Otwinowski and Minor, 1997). For the WT structure, phases were calculated by molecular replacement with the program PHASER (McCoy et al., 2007), using the structure of TaGGR (PDB ID: 3OZ2) (Xu et al., 2010) as a search model. Automated model building was conducted using Autobuild (Terwilliger, 2003) from the PHENIX suite of programs (Adams et al., 2010) resulting in a model that was 85% complete. Manual building using Coot (Emsley and Cowtan, 2004) was alternated with reciprocal space refinement using PHENIX (Afonine et al., 2012). Waters were automatically placed using PHENIX and manually added or deleted with Coot according to peak height (>3.0 σ in the F_o-F_c map) and the distance to a potential hydrogen bonding partner (< 3.5 Å). TLS refinement (Winn et al., 2001) of 10 groups, chosen by the TLSMD web server (Painter and Merritt, 2006), was used in later rounds of refinement. All mutant structures were refined and built in the same manner as the WT model. All data collection, phasing, and refinement statistics are summarized in Table 1.

References

Adams, P.D., Afonine, P.V., Bunkóczi, G., Chen, V.B., Davis, I.W., Echols, N., Headd, J.J., Hung, L.-W., Kapral, G.J., Grosse-Kunstleve, R.W., McCoy, A.J., Moriarty, N.W., Oeffner, R., Read, R.J., Richardson, D.C., Richardson, J.S., Terwilliger, T.C., and Zwart, P.H. (2010). PHENIX: a comprehensive Python-based system for macromolecular structure solution. Acta Crystallogr *D66*, 213-221.

Afonine, P.V., Grosse-Kunstleve, R.W., Echols, N., Headd, J.J., Moriarty, N.W., Mustyakimov, M., Terwilliger, T.C., Urzhumtsev, A., Zwart, P.H., and Adams, P.D. (2012). Towards automated crystallographic structure refinement with *phenix.refine*. Acta Crystallogr *D68*, 352-367.

Ajikumar, P.K., Xiao, W.H., Tyo, K.E.J., Wang, Y., Simeon, F., Leonard, E., Mucha, O., Phon, T.H., Pfeifer, B., and Stephanopoulos, G. (2010). Isoprenoid Pathway Optimization for Taxol Precursor Overproduction in *Escherichia coli*. Science *330*, 70-74.

Alper, H., Miyaoku, K., and Stephanopoulos, G. (2005). Construction of lycopene-overprducing *E. coli* strains by combining systematic and combinatorial gene knockout targets. Nat Biotechnol *23*, 612-616.

Bradford, M.M. (1976). A rapid and sensitive method for the quantitation of microgram quantities of protein utilizing the principle of protein-dye binding. Anal Biochem *72*, 248-254.

Emsley, P., and Cowtan, K. (2004). Coot: model-building tools for molecular graphics. Acta Cryst *D60*, 2126-2132.

Farmer, W.R., and Liao, J.C. (2000). Improving lycopene production in *Escherichia coli* by engineering metabolic control. Nat Biotechnol *18*, 533-537.

Jancarik, J., and Kim, S.-H. (1991). Sparse matrix sampling: a screening method for crystallization of proteins. J Appl Cryst *24*, 409-411.

McCoy, A.J., Grosse-Kunstleve, R.W., Adams, P.D., Winn, M.D., Storoni, L.C., and Read, R.J. (2007). *Phaser* Crystallographic Software. J Appl Cryst *40*, 658-674.

Nishimura, Y., and Eguchi, T. (2006). Biosynthesis of archaeal membrane lipids: digeranylgeranylglycerophospholipid reductase of the thermoacidophilic archaeon *Thermoplasma acidophilum*. J Biochem *139*, 1073-1081.

Otwinowski, Z., and Minor, W. (1997). Processing of X-ray diffraction data collected in oscillation mode. Methods Enzymol *276*, 307-326.

Painter, J., and Merritt, E.A. (2006). *TLSMD* web server for the generation of multi-group TLS models. J Appl Cryst *39*, 109-111.

Peralta-Yahya, P.P., Ouellet, M., Chan, R., Mukhopadhyay, A., Keasling, J.D., and Lee, T.S. (2011). Identification and microbial production of a terpene-based advanced biofuel. Nat Commun *2*, 483.

Renninger, N.S., and McPhee, D.J. (2008). Fuel compositions comprising farnesane and farnesane derivatives and method of making and using same. US patent 7399323.

Ro, D.-K., Paradise, E.M., Ouellet, M., Fisher, K.J., Newman, K.L., Ndungu, J.M., Ho, K.A., Eachus, R.A., Ham, T.S., Kirby, J.*, et al.* (2006). Production of the antimalarial drug precursor artemisinic acid in engineered yeast. Nature *440*, 940-943.

Sasaki, D., Fujihashi, M., Iwata, Y., Murakami, M., Yoshimura, T., Hemmi, H., and Miki, K. (2011). Structure and mutation analysis of archaeal geranylgeranyl reductase. J Mol Biol *409*, 543-557.

Sato, S., Murakami, M., Yoshimura, T., and Hemmi, H. (2008). Specific partial reduction of geranylgeranyl diphosphate by an enzyme from the thermoacidophilic archaeon *Sulfolobus acidocaldarius* yields a reactive prenyl donor, not a dead-end product. J Bacteriol *190*, 3923-3929.

Terwilliger, T.C. (2003). Automated main-chain model building by template matching and iterative fragment extension. Acta Cryst *D59*, 38-44.

Winn, M.D., Isupov, M.N., and Murshudov, G.N. (2001). Use of TLS parameters to model anisotropic displacements in macromolecular refinement. Acta Cryst *D57*, 122-133.

Xu, Q., Eguchi, T., Mathews, I.I., Rife, C.L., Chiu, H.-J., Farr, C.L., Feuerhelm, J., Jaroszewski, L., Klock, H.E., Knuth, M.W.*, et al.* (2010). Insights into substrate specificity of geranylgeranyl reductases revealed by the structure of digeranylgeranylglycerophospholipid reductase, an essential enzyme in the biosynthesis of archaeal membrane lipids. J Mol Biol *404*, 403-417.

AUTHOR CONTRIBUTION

Y.K. constructed SaGGR variants, expressed and purified protein samples, and performed kinetic studies. R.P.M. performed crystallographic structure determination and analysis, with the aid of J.H.P. Initial SaGGR work was performed by C.C.L. and X.X., who determined temperature and pH dependence. Y.K. and R.P.M. wrote the manuscript, and all authors were involved in study design.

ACKNOWLEDGEMENTS

We thank Edward Baidoo for his help with LC-TOF MS data collection, Sharon Borglin for fatty acid methyl ester (FAME) analysis, and Hanbin Liu for computer simulation. This work was part of the DOE Joint BioEnergy Institute (JBEI), which is funded by the U. S. Department of Energy, Office of Science, Office of Biological and Environmental Research, through contract DE-AC02-05CH11231 between Lawrence Berkeley National Laboratory and the U. S. Department of Energy. The Berkeley Center for Structural Biology is supported in part by the National Institutes of Health, National Institute of General Medical Sciences, and the Howard Hughes Medical Institute. The Advanced Light Source is supported by the Director, Office of Science, Office of Basic Energy Sciences, of the U.S. Department of Energy under Contract No. DE-AC02-05CH11231. J.D.K. has financial interests in Amyris and LS9.

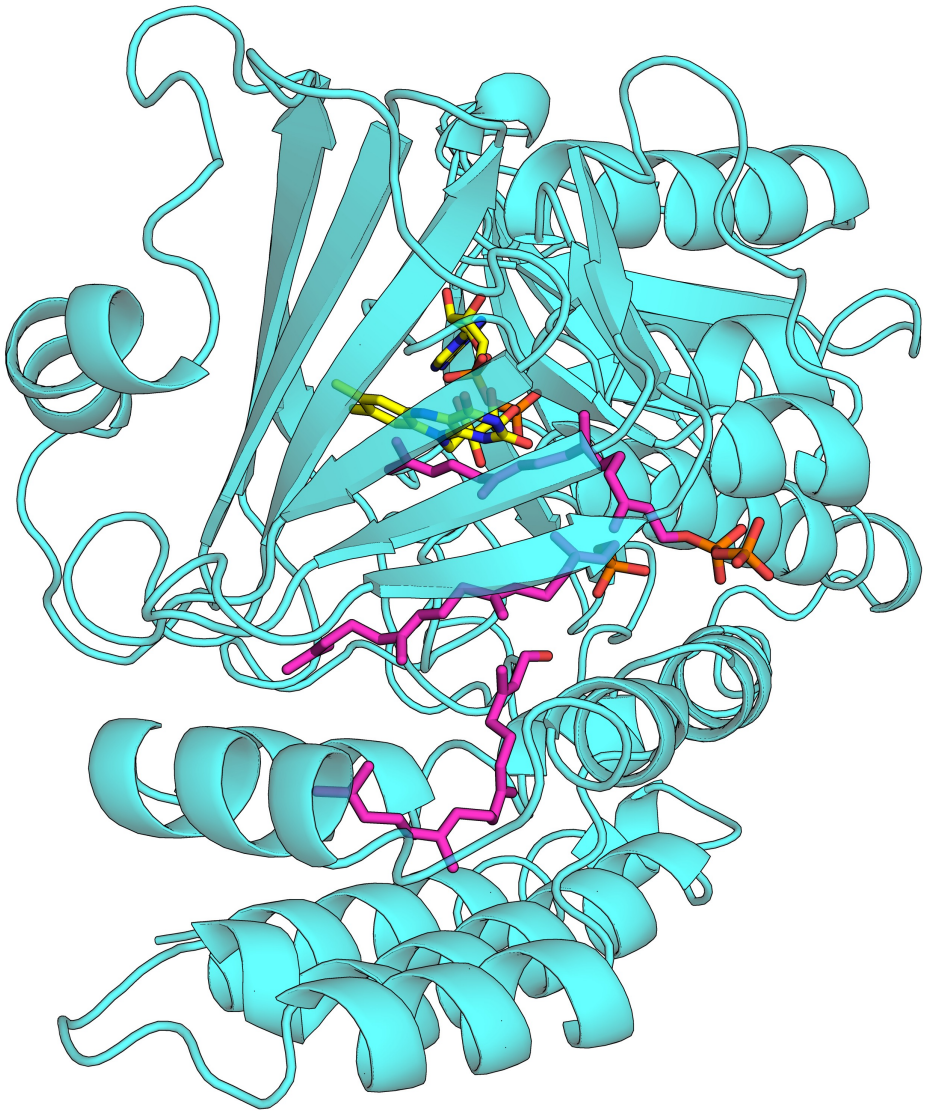

Figure 1. Overall fold of SaGGR. The structure of SaGGR was solved to high resolution bound with GGPP (magenta). SaGGR is a monomer composed of two functional domains, an FAD (yellow) binding Rossmann-type fold domain (residues 1-74) and a ligand–binding domain (residues 75-453). Protein in cyan ribbons and FAD (C in yellow) and GGPP (C in magenta) shown in sticks, with O in red, N in blue, and P in orange.

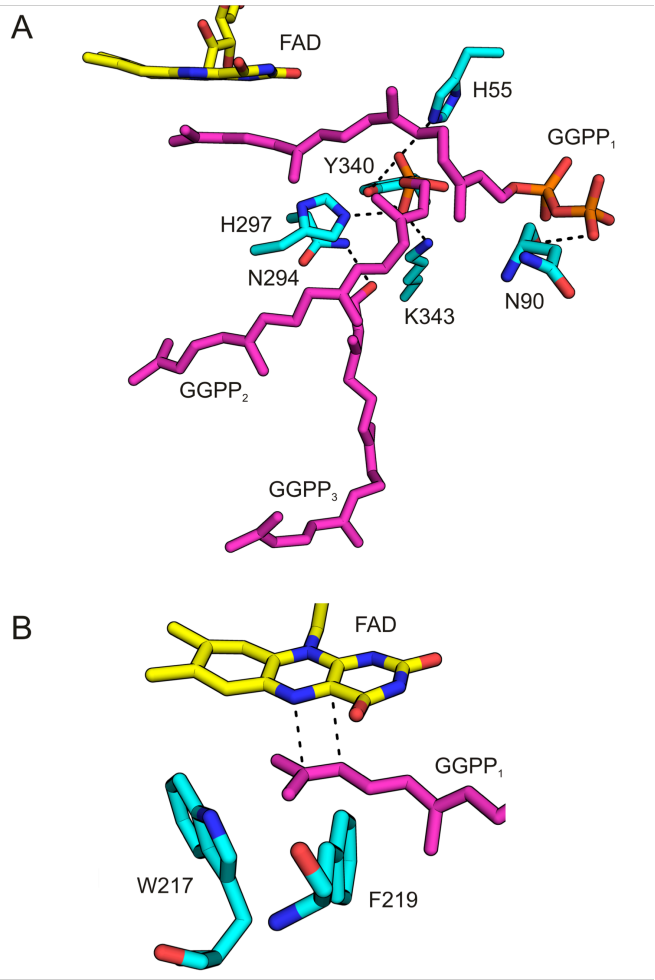

Figure 2. Active site of SaGGR. (A) SaGGR was co-crystallized with GGPP. Electron density was resolved for three separate molecules of GGPP (Figure S2). Like PG, only one chain ($GGPP_1$), appears to be bound in a catalytically competent manner, with its Δ^{14} double bond proximal to N^5 of FAD. The hydrophobic chain from the second molecule ($GGPP_2$) is bound in a similar manner as the second chain from PG. The third molecule ($GGPP_3$) binds SaGGR alongside $GGPP_2$ within the same cavity. (B) The SaGGR active site showing the FAD isoalloxazine ring, the $GGPP_1$ Δ^{14} double bond, and conserved residues W217 and F219. FAD (C in yellow), GGPP (C in magenta), and protein residues (C in cyan) shown in sticks, with O in red, N in blue, and P in orange.

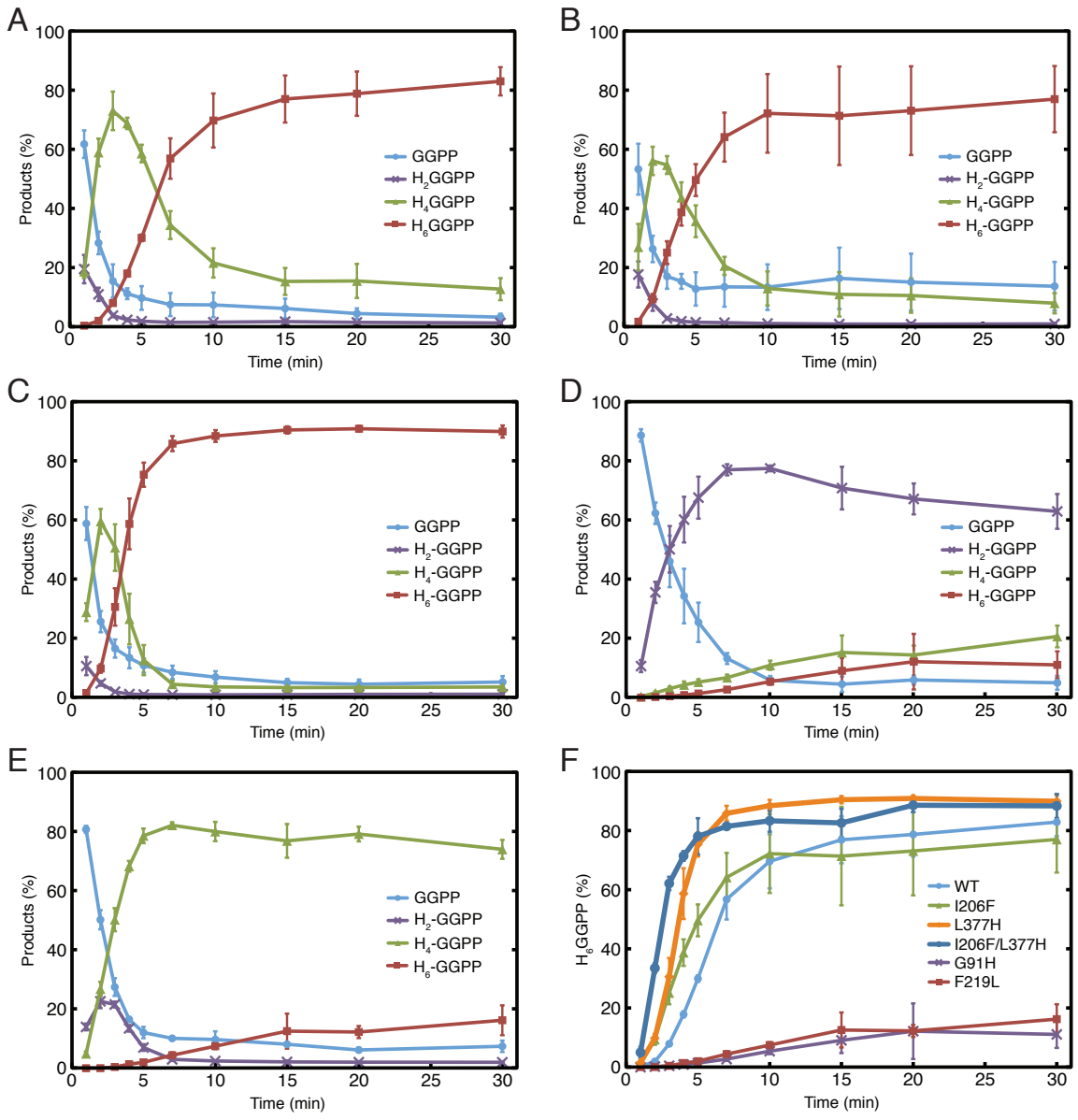

Figure 3. Distribution of WT and mutant SaGGR reaction products over time. Reaction products for (A) WT, (B) I206F, (C) L377H, (D) G91H, and (E) F219L SaGGR. (F) Time-dependent formation of H_6GGPP from GGPP for WT and mutant SaGRR. WT, I206F, L377H, and I206F/L377H SaGGR produce H_6GGPP as the final product. However, the primary products of the G91H and F219L mutants are H_2GGPP and H_4GGPP, respectively. The apparent rate of GGPP reduction to H_6GGPP was enhanced in I206F, L377H, and I206F/L377H mutants compared to the WT.

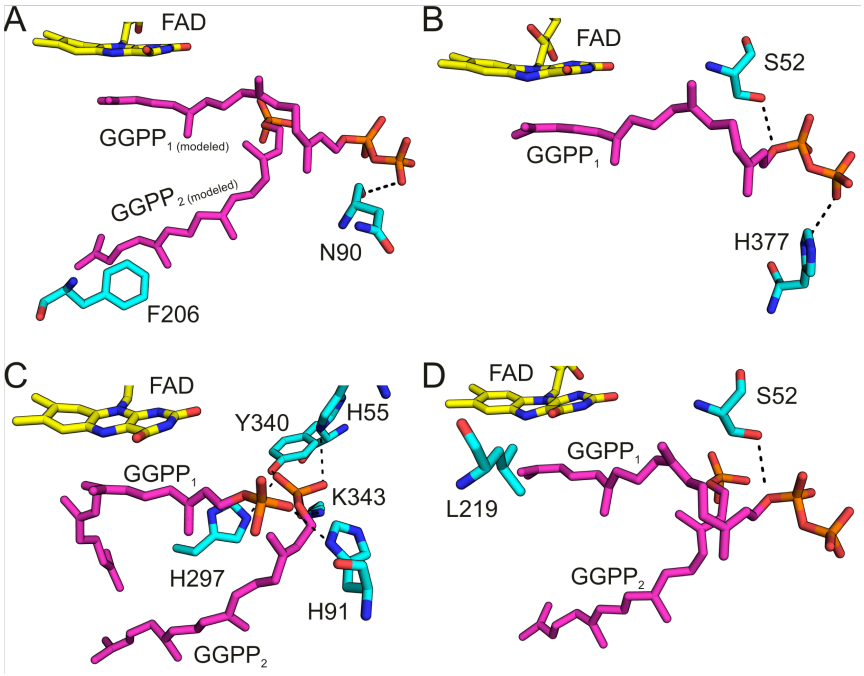

Figure 4. Active sites of engineered SaGGR variants. (A) The I206F mutant shows increased activity compared to WT SaGGR. $GGPP_1$ and $GGPP_2$ are not present in this structure but have been modeled in to demonstrate that F206 partially occludes the second cavity. Therefore, this catalytically inactive binding conformation is unavailable to GGPP. I206 from the WT structure (orange) has been overlaid with F206 to demonstrate the steric hindrance caused by the introduction of a bulky phenylalanine. (B) The L377H mutant shows improved activity over WT and I206F and reduces 3 of the 4 GGPP double bonds. H377 forms a salt bridge with the GGPP pyrophosphate. (C) The G91H mutant reduces only one GGPP double bond. H91 forms a salt bridge with the GGPP pyrophosphate, with the Δ^6 double bond adjacent the N_5 of FAD. (D) The F219L mutant only reduces two GGPP double bonds. The mutation increases the size of the active site cavity and may no longer provide sufficient van der Waals interactions for efficient binding and reduction of substrate. FAD (C in yellow), GGPP (C in magenta), and protein residues (C in cyan) shown in sticks, with O in red, N in blue, and P in orange.

Table 1. X-ray data collection and refinement statistics.

	SaGGR	GGPP	G91H	I206F	L377H	F219L	I206F/L377H
PDB ID	4OPC	4OPD	4OPU	4OPL	4OPG	4OPI	4OPT
Resolution (Å)	50 -1.4 (1.42 -1.4)	50 - 1.83 (1.86 - 1.83)	50 – 2.70 (2.75 – 2.70)	50 – 2.48 (2.52-2.48)	50 – 2.07 (2.11-2.07)	50 – 2.24 (2.28-2.24)	50 – 2.60 (2.64-2.60)
Space group	C 1 2 1	P 1	P 2 1 2 1 2 1	P 2 1 2 1 2 1	P 2 1 2 1 2 1	P 2 1 2 1 2 1	P 2 1 2 1 2 1
Unit cell (Å)	a = 109.0 b = 65.3 c = 63.2 α = γ = 90° β = 92.0°	a = 63.1 b = 63.2 c = 65.1 α = 121.0° β = 90.0° γ = 88.6°	a = 63.9 b = 82.0 c = 106.2 α = β = γ = 90°	a = 65.3 b = 78.9 c = 106.0 α = β = γ = 90°	a = 63.2 b = 81.7 c = 105.9 α = β = γ = 90°	a = 63.8 b = 83.0 c = 106.4 α = β = γ = 90°	a = 63.7 b = 82.2 c = 106.4 α = β = γ = 90°
Total reflections	511159	272344	153053	181226	328857	186897	121720
Unique reflections	83434	75985	15943	19915	34256	27895	17900
Multiplicity	6.1 (4.5)	3.6 (2.6)	9.6 (8.3)	9.1 (5.7)	9.6 (8.0)	6.7 (5.4)	6.8 (5.5)
Completeness (%)	96.60 (82.40)	97.30 (93.4)	98.7 (87.2)	97.4 (77.1)	100.0 (99.9)	99.3 (93.5)	98.0 (81.4)
I/sigma(I)	33.7 (1.92)	11.1 (1.15)	17.8 (1.46)	28.5 (1.53)	27.7 (1.82)	23.0 (2.87)	15.3 (1.43)
R-sym	0.039 (0.506)	0.107 (0.547)	0.122 (0.892)	0.103 (0.644)	0.075 (0.890)	0.068 (0.547)	0.110 (0.816)
R-factor	0.15	0.15	0.21	0.26	0.19	0.19	0.19
R-free	0.18	0.19	0.25	0.29	0.21	0.23	0.22
RMS from ideal geometry							
Bonds (Å)	0.006	0.007	0.002	0.002	0.002	0.002	0.002
Angles (°)	1.1	1.064	0.723	0.564	0.612	0.716	0.575
Ramachandran plot							
Favored (%)	99	98	98	98	98	98	97
Outliers (%)	0	0.2	0	0	0	0	0
Clashscore	1.98	3.83	4.22	2.91	1.9	1.91	2.47

Statistics for the highest-resolution shell are shown in parentheses.

Table 2. Kinetic data for wild-type SaGGR and its engineered mutants.

SaGGR variant	Product	v_{app} (μM min^{-1})	k_{app} (min^{-1})	t_{50} (min)
WT	H_6GGPP	12 ± 2	0.40 ± 0.05	6.3
I206F	H_6GGPP	16 ± 4	0.53 ± 0.14	5.0
L377H	H_6GGPP	28 ± 11	0.94 ± 0.36	3.7
I206F/L377H	H_6GGPP	29 ± 3	0.95 ± 0.09	2.6
G91H	H_2GGPP	25 ± 4	0.83 ± 0.14	3.0
F219L	H_4GGPP	23 ± 5	0.78 ± 0.15	3.0

Note: v_{app}, k_{app}, and t_{50} are the apparent rate, the apparent rate constant, and the time to reach 50% maximal conversion from GGPP, respectively, for the products indicated.

Supplemental Information

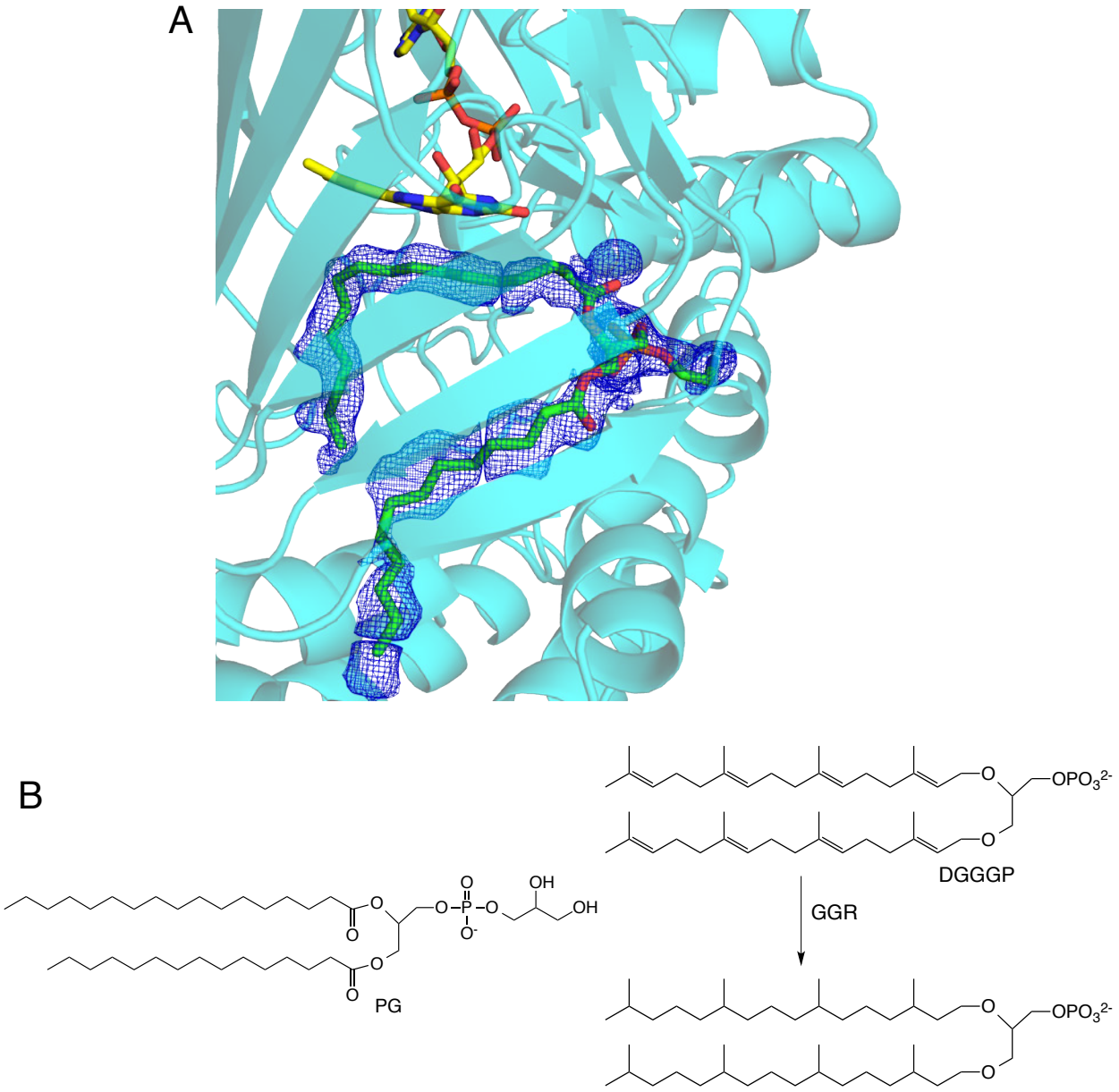

Figure S1, related to Figure 1. Binding of phosphatidylglycerol (PG) to SaGGR. (A) Protein in cyan ribbons and FAD (C in yellow) and PG (C in green) in sticks (O in red, O in blue, P in orange). $2F_O–F_C$ density around PG in blue mesh contoured at 1 σ. (B) The structure of PG in the model compared to 2,3-di-*O*-geranylgeranylglyceryl phosphate (DGGGP), the native GGR substrate.

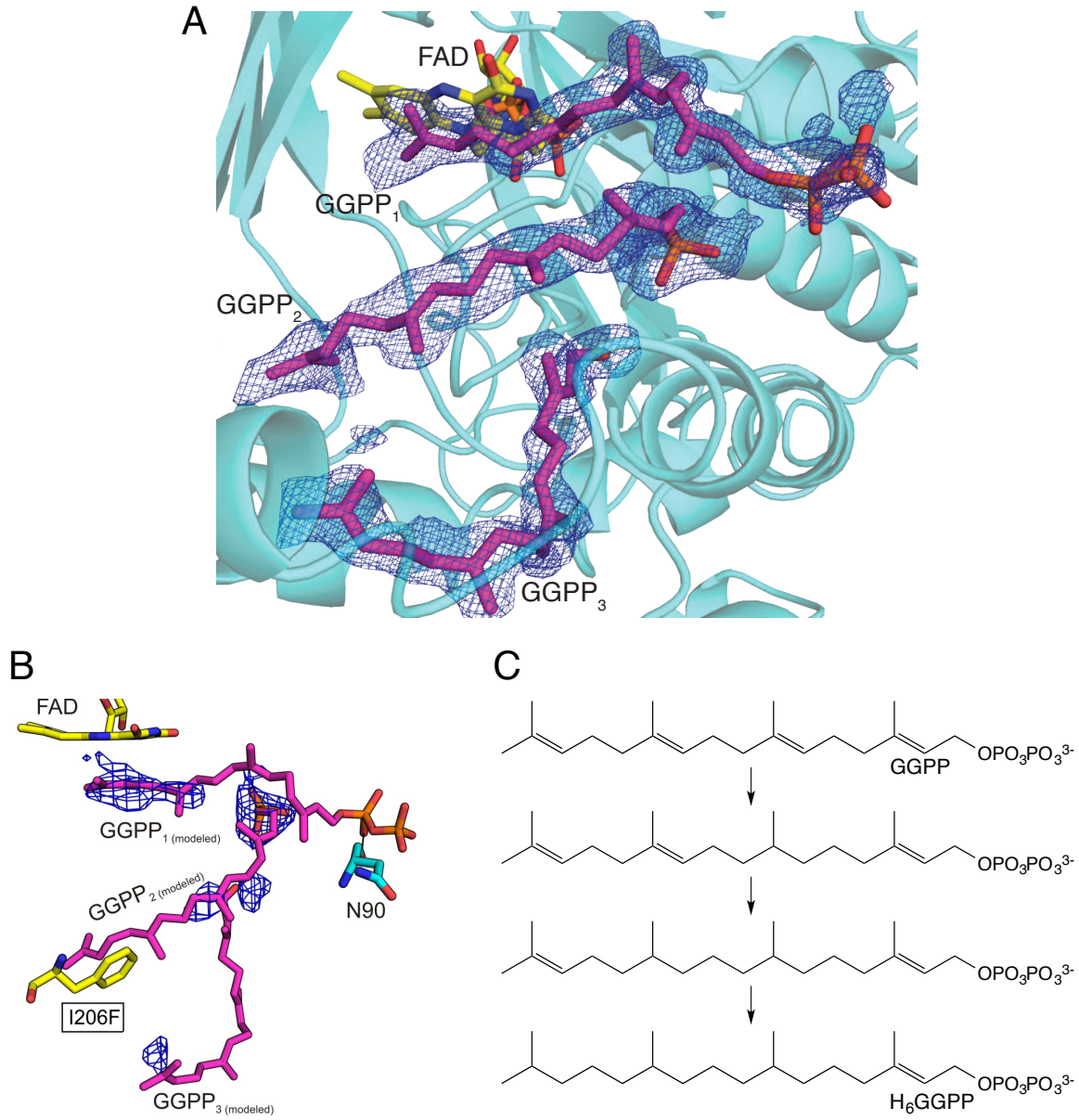

Figure S2, related to Figures 1, 2, and 4. The GGPP binding sites of SaGGR. (A) Of the three GGPP molecules bound, only one ($GGPP_1$) represents a catalytically relevant binding site, with the Δ^{14} double bond positioned adjacent the N^5 of FAD for reduction. Electron density for the entire pyrophosphate moieties of $GGPP_2$ and $GGPP_3$ was insufficient to model these head groups. Protein in cyan ribbons and FAD (C in yellow) and GGPP (C in magenta) in sticks (O in red, O in blue, P in orange). $2F_O–F_C$ density around GGPP molecules in blue mesh (1 σ). (B) $2F_O–F_C$ omit density (blue mesh, 1 σ) in

GGPP-binding regions of the I206F SaGGR mutant. Although some weak density is present, it is insufficient to include GGPP in the final model. Instead, the GGPP-binding locations are shown based on the GGPP positions in the WT SaGGR structure. It should be noted that strong density is observed near the phosphate head group of $GGPP_2$. It is possible that in the absence of $GGPP_2$ a phosphate ion has bound to this position. (C) The structure of GGPP and the proposed SaGGR-catalyzed stepwise reduction to H_6GGPP.

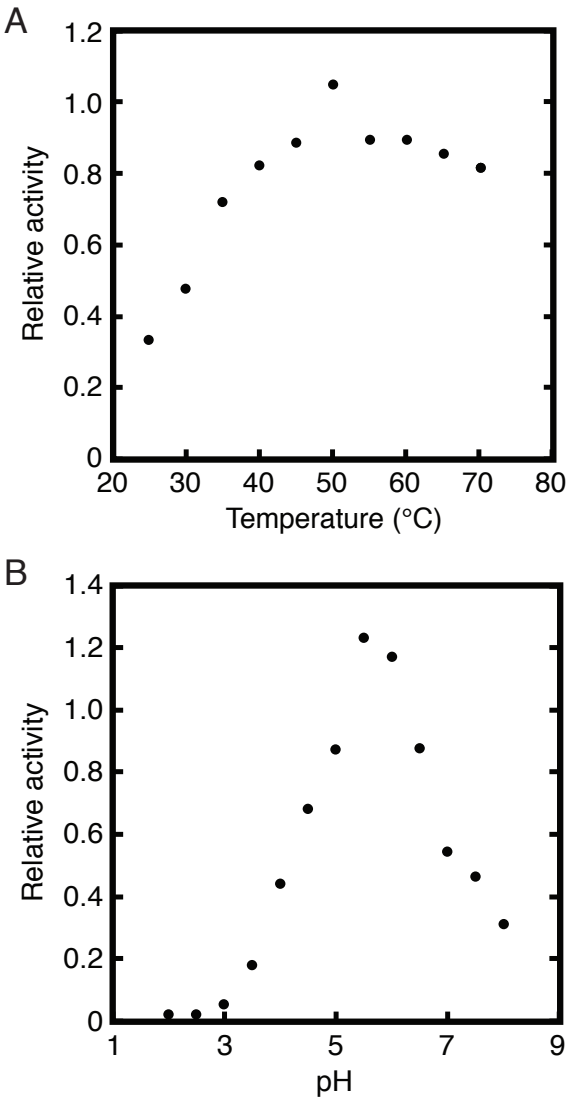

Figure S3, related to Figure 3 and Table 2. Temperature and pH optima for WT SaGGR. (A) The optimal temperature for the enzyme appeared at about 55°C, while (B) the pH optimum was at about 5.5.

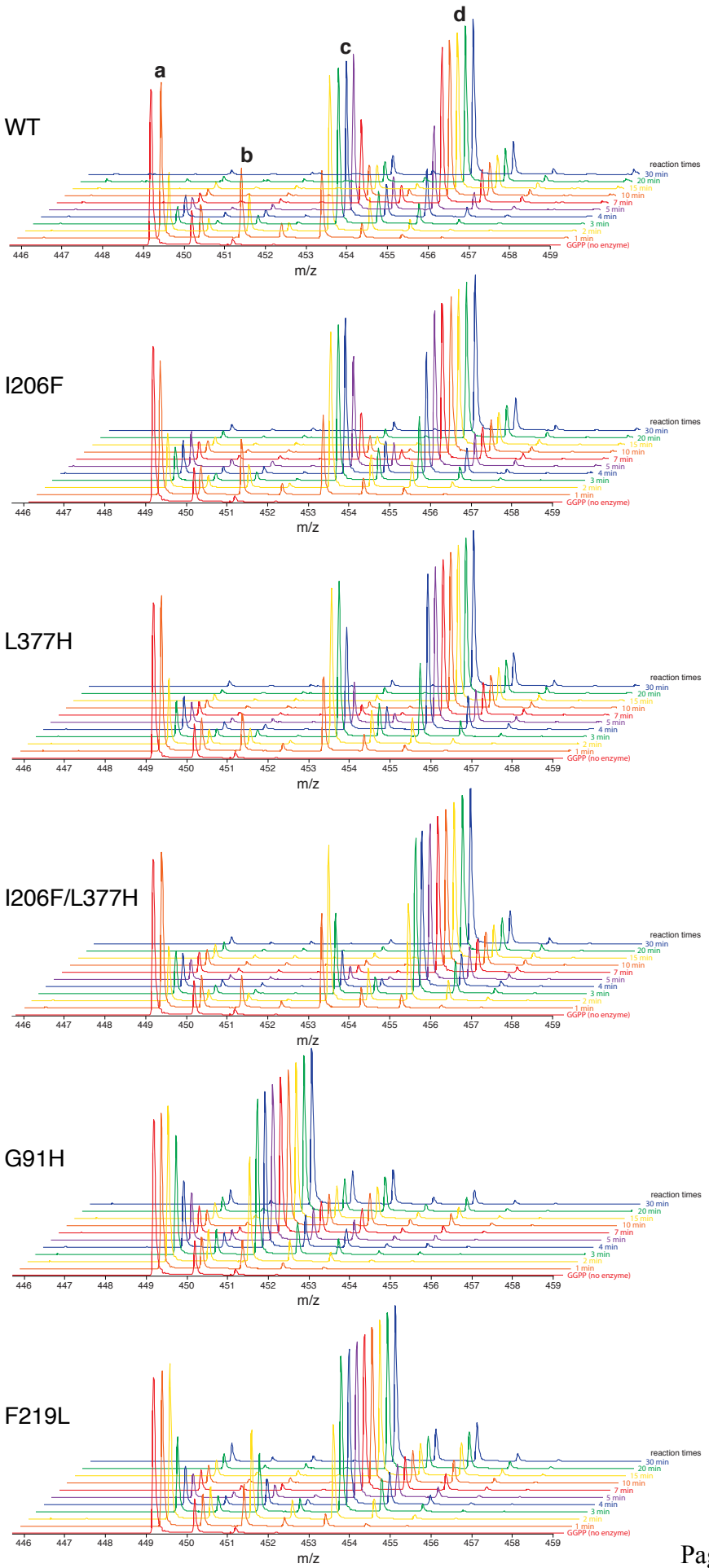
WT
a
b
c
d
I206F
L377H
I206F/L377H
G91H
F219L
reaction times
30 min
20 min
15 min
10 min
7 min
5 min
4 min
3 min
2 min
1 min
GGPP (no enzyme)
446 447 448 449 450 451 452 453 454 455 456 457 458 459
m/z

Figure S4, related to Figures 3 and 4 and Table 2. Representative mass spectrometry data from WT and mutant SaGGR enzymatic activity experiments, determined by LC-TOF MS. The mass spectrum for the GGPP-only control without added enzyme (bottom, red line) shows a single species representing unreacted GGPP (parent peak **a**, m/z: 449.2; additional peaks observed in this spectrum represent GGPP isotopic peaks [M+1], [M+2], etc.). In the enzymatic assay with WT SaGGR, GGPP is rapidly consumed to form the singly-reduced intermediate H_2GGPP (parent peak **b**, m/z: 451.2) before formation of the H_4GGPP intermediate (parent peak **c**, m/z: 453.2). Following a build-up of H_4GGPP, further reduction to H_6GGPP (parent peak **d**, m/z: 455.2) ensued, which is the final product. The fully reduced H_8GGPP product (expected m/z: 457.2) was not observed. Data for mutant SaGGR are also shown, depicting the reduction of GGPP to H_6GGPP for I206F, L377H, and I206F/L377H mutants. However, GGPP reduction terminates at H_2GGPP and H_4GGPP for the G91H and F219L SaGGR mutants, respectively.

Table S1, related to Figures 3 and 4 and Table 2. Oligonucleotide primers used for the generation of SaGGR mutants. Mutant codons are capitalized. The reverse primers used contain the reverse complementary sequence of the forward primers below. The I206F/L377H mutant was generated using the L377H oligonucleotide primer and the I206F mutant sequence as the template.

Mutant	Forward primer (5′-)
I206F	gaggaccatgactacttgagaatattcTTTgatcaagagacatctccaggc
L377H	aagaagaagattataaaagaagaggatctgCATgaagcaagtgaaaaaggagatcttca
G91H	gatatgcagacagtatggacagtaaatCATgagggttttgaactaaatgccc
F219L	ccaggcggttattggtggtacCTGcctaaagggaagaacaaag